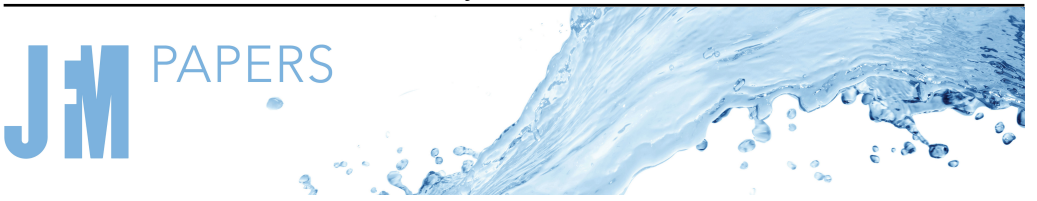
J. Fluid Mech. (2026), *vol.* 1036, A57, doi:10.1017/jfm.2026.11679



Suppression of low-frequency unsteadiness in shock wave–turbulent boundary layer interactions with a micro-bump

Zhen Zhang[1] **and Jiaao Hao**[1]

[1]Department of Aeronautical and Aviation Engineering, The Hong Kong Polytechnic University, Kowloon, Hong Kong

Corresponding author: Jiaao Hao, jiaao.hao@polyu.edu.hk

(Received 27 October 2025 UTC; revised 31 March 2026 UTC; accepted 8 May 2026 UTC)

We propose a novel flow-control strategy to suppress low-frequency unsteadiness in shock wave–turbulent boundary layer interactions. Our analysis reveals that the breathing motion of the separation bubble is governed by the leading two-dimensional global mode through a modal resonance mechanism, with its growth rate primarily concentrated in a narrow region near the shock foot. By introducing a micro-bump at this critical location, we achieve targeted stabilisation of the global mode, resulting in a substantial attenuation of the low-frequency breathing motion. Consequently, the turbulent kinetic energy and wall-pressure fluctuations associated with the breathing motion are reduced by 85 % and 70 %, respectively. This study demonstrates an effective and precise approach for controlling low-frequency unsteadiness in shock-induced separation, while minimally disturbing the flow.

Key words: supersonic flow, instability control

1. Introduction

Shock wave–turbulent boundary interactions (STBLIs) are prevalent in high-speed flows, such as those over transonic wings, in supersonic inlets and in over-expanded nozzles. A well-documented phenomenon in such flows is the low-frequency intermittent shock motion, often referred to as the breathing motion of turbulent separation bubbles (Souverein *et al.* 2010; Clemens & Narayanaswamy 2014). These motions can couple with adjacent structures and generate unsteady aerodynamic loads, posing significant risks to

© The Author(s), 2026. Published by Cambridge University Press. This is an Open Access article, distributed under the terms of the Creative Commons Attribution licence (https://creativecommons.org/licenses/by/4.0/), which permits unrestricted re-use, distribution and reproduction, provided the original article is properly cited.

https://doi.org/10.1017/jfm.2026.11679 Published online by Cambridge University Press

the structural integrity of an airframe (Dolling 2001). This concern has motivated growing research interest in flow-control strategies aimed at mitigating the hazards associated with STBLIs.

Babinsky & Ogawa (2008) classified the control strategies into two main categories: boundary-layer control and shock control. Boundary-layer control aims to delay separation by modifying the upstream boundary layer, whereas shock control focuses on altering the shock structure itself. Vortex generators are widely used for boundary-layer control, producing trailing vortices that enhance momentum exchange to delay flow separation (Anderson, Tinapple & Surber 2006; Ghosh, Choi & Edwards 2008; Sun *et al.* 2019). Despite their ability to introduce strong three-dimensional (3-D) effects and alter the upstream boundary layer, they may not effectively suppress the inherent low-frequency unsteadiness of STBLIs. In fact, Della Posta *et al.* (2024) reported that upstream vortex generators even enhanced this unsteadiness. Shock-control bumps, on the other hand, are commonly applied to transonic wings, as comprehensively reviewed by Bruce & Colliss (2015), with research emphasis placed on drag reduction and shock buffet delay. In shock impingement interactions, bumps are often employed to suppress flow separation (Nastro *et al.* 2023; Ribeiro & Taira 2024). More recently, Ceci (2025) shifted the focus towards attenuating the two-dimensional (2-D) low-frequency unsteadiness of the turbulent separation bubble. Through direct numerical simulations, they demonstrated that a bump shaped as the dividing streamline topology of the uncontrolled interaction can effectively eliminate flow separation and suppress low-frequency breathing motion, if appropriately positioned.

Despite these advances, most control strategies rely on trial-and-error and often introduce extra drag due to significant geometric change. This limitation stems from the incomplete physical understanding of the breathing motion, which, as noted by Clemens & Narayanaswamy (2014), is governed by coupled upstream and downstream mechanisms. Recently, a promising explanation has been proposed through stability analysis: the unsteadiness is intrinsic, governed by a 2-D global mode that is excited by external disturbances (Touber & Sandham 2009; Nichols *et al.* 2017; Hao 2023). This insight enables a more targeted control methodology, referred to as stability-based control, focusing on the suppression of the global mode itself. In this context, stability-based control has gained traction recently (Marquet, Sipp & Jacquin 2008; Martinez-Cava *et al.* 2020; Nastro *et al.* 2023; Ribeiro & Taira 2024; Jung, Bhagwat & Towne 2025), owing to its physics-informed foundation, computational efficiency and straightforward implementation. A representative example is the work of Martinez-Cava *et al.* (2020), who proposed a micro-bump for the control of shock buffet using stability-based control. Transonic buffet is a self-sustained oscillation governed by an unsteady, globally unstable mode. Motivated by this approach, the present study aims to employ a similar stability-based control strategy to suppress the low-frequency breathing motion.

In this study, using large-eddy simulation (LES) and global stability analysis (GSA), we identify the sensitive region of the leading 2-D global mode, design and position a micro-bump accordingly and effectively suppress the low-frequency breathing motion in a supersonic compression ramp flow.

2. Numerical strategies

2.1. *Geometry and free-stream parameters*

A 25° compression ramp is considered. A Cartesian coordinate system is adopted with its origin fixed at the corner. The streamwise, vertical and spanwise directions are denoted by

https://doi.org/10.1017/jfm.2026.11679 Published online by Cambridge University Press

x, y and z, respectively, with the corresponding velocity components given by u, v and w. The free-stream parameters are as follows: density $\rho_\infty = 0.314\,\mathrm{kg\,m^{-3}}$, Mach number $M_\infty = 2.95$, temperature $T_\infty = 108\,\mathrm{K}$ and Reynolds number $Re_\delta = 63\,500$ based on the boundary-layer thickness δ at the reference station $x = -15.4\delta$. The flow is modelled as a perfect gas with a specific heat ratio of 1.4 and a Prandtl number of 0.72. The molecular viscosity μ is calculated using Sutherland's law.

2.2. *Computational set-up*

Implicit LES are conducted using an in-house solver named PHAROS (Hao & Wen 2020). The inviscid fluxes are computed using a sixth-order skew-symmetric central difference scheme (Pirozzoli 2010) in smooth-flow regions. In regions containing discontinuities, the scheme is switched to the AUSM$^+$-up scheme (Liou 2006) with a fifth-order weighted essentially non-oscillatory reconstruction (Jiang & Shu 1996). The switching is controlled by a modified Jameson sensor (Jameson, Schmidt & Turkel 1981), with a threshold of 0.1. The viscous terms are discretised using a second-order central difference scheme, and time integration is carried out with a third-order Runge–Kutta method.

Turbulent inflow is generated using the modified digital filter technique (Touber & Sandham 2009). A non-reflective boundary condition (Mani 2012) is applied at the upper domain boundary, while the outflow boundary uses a simple extrapolation, which is located far downstream of the interaction region with a stretched grid applied as a sponge zone. The streamwise distance between the outflow boundary and the corner is approximately 20δ, while the sponge zone lasts for 6δ. The wall is treated as isothermal with a fixed temperature of $T_w = 275.4\,\mathrm{K}$. Periodic boundary conditions are imposed in the spanwise direction, which has a width of 4δ. Although this domain width is insufficient to resolve the large-scale 3-D spanwise undulations reported in recent numerical and experimental studies (Ceci *et al.* 2023; Liu *et al.* 2024), Zhang *et al.* (2025*b*) showed that the quasi-2-D breathing motion is the dominant factor in wall-pressure response. This conclusion is supported by several numerical investigations demonstrating that experimental wall-pressure fluctuations can be accurately reproduced with comparably narrow computational domains (Pasquariello, Hickel & Adams 2017; Fang *et al.* 2020; Bernardini *et al.* 2023). A detailed discussion of the effects of spanwise widths is provided in Appendix A. At the reference station, the grid resolutions in wall units are approximately $\Delta x^+ \approx 19$, $\Delta y_w^+ \approx 1.0$ and $\Delta z^+ \approx 10$. For the solver validation, the reader is referred to Zhang *et al.* (2025*b*).

2.3. *Global stability analysis*

The linearised Navier–Stokes equation in the operator form is written as

$$\frac{\partial \boldsymbol{U'}}{\partial t} = \boldsymbol{\mathcal{A}}\boldsymbol{U'}, \tag{2.1}$$

where $\boldsymbol{U'}$ is a small-amplitude 3-D perturbation vector and $\boldsymbol{\mathcal{A}}$ is the linearised Navier–Stokes operator. The perturbation term is assumed in the following modal norm:

$$\boldsymbol{U'}(x, y, z, t) = \hat{\boldsymbol{U}}(x, y)\exp\left[i\beta z - i(\omega_r + i\omega_i)t\right], \tag{2.2}$$

where $\hat{\boldsymbol{U}}$ is the 2-D function, β represents the spanwise wavenumber, ω_r denotes the angular frequency and ω_i indicates the growth rate. Here $\omega_i > 0$ means a flow is globally unstable (and vice versa). Substituting (2.2) into (2.1) leads to an eigenvalue problem, which can be solved using an in-house GSA solver as described in Hao (2023). Note that an effective viscosity $\mu_{eff} = \mu_t + \mu$ is adopted, where μ_t is the eddy viscosity

https://doi.org/10.1017/jfm.2026.11679 Published online by Cambridge University Press

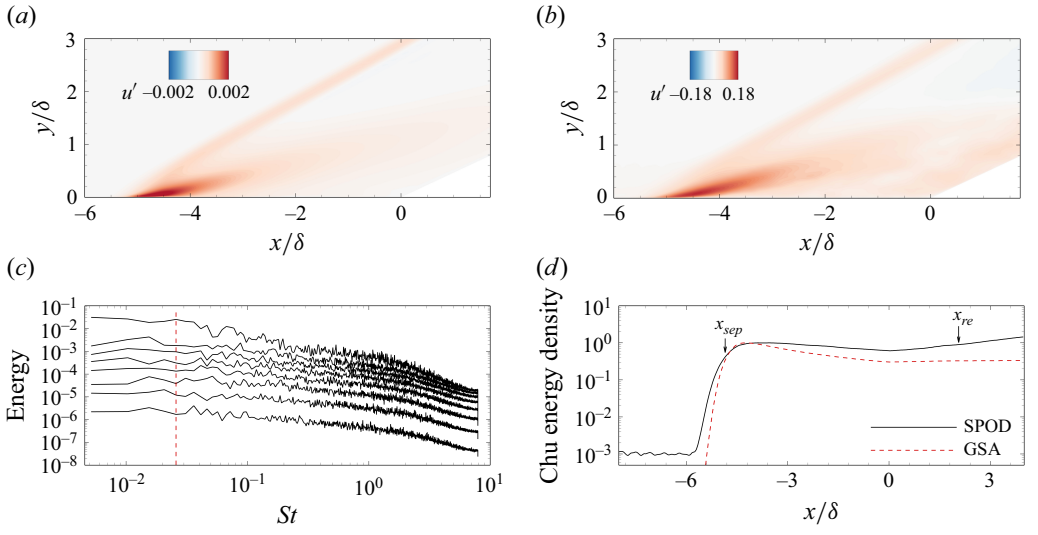


Figure 1. Real parts of (*a*) the 2-D global mode and (*b*) the leading 2-D SPOD mode at $St = 0.026$. (*c*) Normalised energy distribution of SPOD modes; the red dashed line marks the frequency $St = 0.026$. (*d*) Wall-normal integrated Chu energy density for the 2-D global mode and and SPOD modes, normalised by their respective maximum values. The SPOD details: Welch method with a Hamming window, eight segments, 75 % overlap, segment length $194 L_{sep}/u_\infty$.

obtained using a least-squares fit method (Lilly 1992). The formulation of μ_t is detailed in Appendix B. A sponge layer is placed near the left boundary (Mani 2012) to avoid any introduction of disturbances, while the remaining boundaries are treated consistently with the LES.

3. Results

3.1. *The low-frequency unsteadiness*

Hao (2023) demonstrated that 2-D shock motion is primarily driven by a 2-D global mode (referred to as the shock mode), characterised by $\beta = 0$ and $\omega_r = 0$, through a modal resonance mechanism. The interpretation, however, relies on Reynolds-averaged Navier–Stokes (RANS) simulations and RANS-based GSA. As a result, direct evidence for the physical existence of the mode was not established. In the present work, this issue is revisited by comparing 2-D coherent structures extracted from LES with the 2-D global mode obtained from LES-based GSA, thereby providing higher-fidelity support for the underlying mechanism. Spectral proper orthogonal decomposition (SPOD) analysis is performed to extract coherent structures from the unsteady spanwise-averaged data. The input data consist of the spanwise-averaged state vector $q' = [\rho', u', v', w', T']$. Welch's method is used with a Hamming window to minimise spectral leakage, segmenting the dataset into eight blocks with 75 % overlap. The Chu energy norm (Chu 1965) is used as the inner product. The use of spanwise-averaged SPOD is appropriate owing to the quasi-2-D character of the shock motion in ramp flows (Clemens & Narayanaswamy 2014). Figure 1(*a*,*b*) compares the 2-D shock mode and the leading 2-D SPOD mode at the normalised frequency $St = f L_{sep}/u_\infty = 0.026$, where L_{sep} is the separation length and u_∞ is the free-stream velocity. Note that L_{sep} from the uncontrolled case is used in the definition of St throughout this study to ensure consistent comparison. This frequency corresponds the energy peak of the SPOD modes in the low-frequency regime, as shown in

https://doi.org/10.1017/jfm.2026.11679 Published online by Cambridge University Press

figure 1(*c*), and aligns well with the characteristic frequency of the shock motion presented later in figure 2(*c*). The shock mode maintains high values of u' near the shock foot and along the separation shock. Notably, the SPOD mode closely resembles the shock mode, with elevated u' values similarly concentrated around the shock foot and along the shock. Convergence of the SPOD modes is discussed in Appendix C.

A quantitative comparison between the two modes can be conducted using two methods. First, the integrated Chu energy density distributions along the streamwise direction are compared, as shown in figure 1(*d*). Both distributions are normalised by their respective peak values located just downstream of the mean separation point x_{sep}. Slightly upstream of x_{sep}, both profiles increase rapidly towards their peaks. Their growth rates and positions closely match. Downstream of these peaks, both distributions exhibit a gradual decline, followed by an increase beyond the corner. Despite minor differences in the decay rates, the overall trends remain highly similar. This consistent behaviour provides compelling evidence that the two modes share fundamental similarities. The second perspective is to make a projection between the two modes, given by

$$\gamma = \frac{\left| \| \hat{\boldsymbol{\Psi}}_{SPOD}(x, y), \hat{\boldsymbol{U}}_{GSA}(x, y) \|_E \right|}{\| \hat{\boldsymbol{\Psi}}_{SPOD}(x, y) \|_E \times \| \hat{\boldsymbol{U}}_{GSA}(x, y) \|_E}, \tag{3.1}$$

where $\hat{\boldsymbol{\Psi}}_{SPOD}(x, y)$ represents the 2-D leading SPOD mode at $St = 0.026$, while $\hat{\boldsymbol{U}}_{GSA}(x, y)$ denotes the shock mode. The notation $\|\cdot\|_E$ means the Chu norm (Chu 1965). A value of $\gamma = 1$ represents a perfect match of the two modes. The projection coefficient between the two modes shown in figure 1(*a*,*b*) is 0.93, indicating a strong correlation between them. This further supports the conclusion that the low-frequency unsteadiness of the turbulent separation bubble is predominantly driven by the shock mode. Moreover, the low-frequency shock motion can be effectively reconstructed by superimposing the leading SPOD mode at $St = 0.026$ onto the mean flow (see supplementary movie available at https://doi.org/10.1017/jfm.2026.11679).

3.2. *Controlled breathing motion with a micro-bump*

Having established the central role of the 2-D global mode in driving the low-frequency unsteadiness, we now turn to its targeted suppression by exploiting its sensitivity distribution. Following Paladini *et al.* (2019), the core of the 2-D instability can be quantified by the complex density $d = \tilde{U}^{\dagger}\hat{U}$, where $\tilde{U}$ is the 2-D adjoint mode and the superscript † refers to the transconjugate. The adjoint mode is computed by solving the adjoint eigenvalue problem. The real part of d represents the local contribution to the growth rate of the zero-frequency shock mode. Note that the integration of d over the computational domain equals 1. Figure 2(*a*) shows the growth rate density map for the shock mode. The highest density values are concentrated near the shock foot, consistent with the mode structure shown in figure 1(*a*). In contrast, the density remains nearly zero elsewhere, including across the separation shock. This localised distribution indicates that the shock-foot region dominates the sensitivity to global instabilities, a finding consistent with Paladini *et al.* (2019) in the research of transonic shock buffet, which is governed by a globally unstable, oscillatory mode.

To mitigate the instability contribution from the shock-foot region, we introduce a local surface modification. Inspired by Martinez-Cava *et al.* (2020), who showed that the optimal surface deformation for weakening shock-buffet instability resembles a shock-control bump, we adopt a similar control bump around the shock-foot region,

https://doi.org/10.1017/jfm.2026.11679 Published online by Cambridge University Press

Case	h	x_l	x_p	x_r	A	B	C	D
C_{35}	0.35 mm	-5.15δ	-4.41δ	-3.74δ	1.7	3	6	-0.3

Table 1. Parameters in (3.2): h, bump height; x_l and x_r, left and right boundaries; x_p, bump peak location; A, B, C and D, shape-control constants.

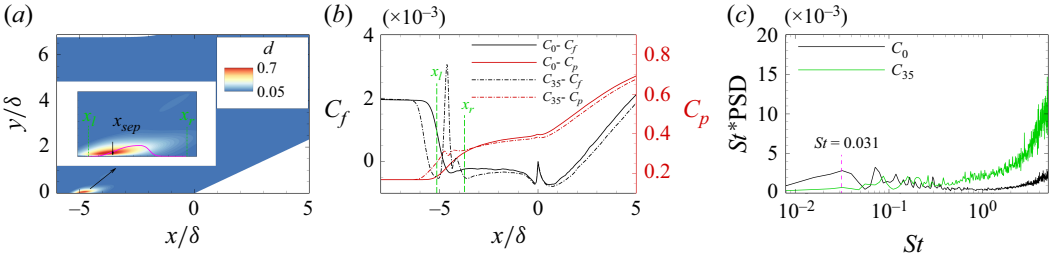


Figure 2. (*a*) Real part of the shock mode's growth rate density map, with the bump edges x_l and x_r marked by green lines. (*b*) Comparison of skin-friction (C_f) and pressure (C_p) coefficients. (*c*) Pre-multiplied wall-pressure spectra at station x_{sep} (case C_0) and station x_p (case C_{35}).

as highlighted by the purple line in the inset of figure 2(*a*). This small-scale bump is designed to control the shock mode and suppress the low-frequency shock motion. The geometric configuration of the bump is defined by the following shape function:

$$y = \begin{cases} h_1 \times (1 - \exp(-(x - x_p + A)^B)) & \text{if } x_l \le x < x_p, \\ h_2 \times (1 - \tanh(C \times (x - x_p + D))) & \text{if } x_p \le x \le x_r. \end{cases} \tag{3.2}$$

Here, $h_1 = h/(1 - \exp(-A^B))$ and $h_2 = h/(1 - \tanh(C \times D))$ are scaling factors, where h is the bump height. The streamwise extent and positioning of the bump are defined by x_l and x_r marking the left and right boundaries, respectively, and x_p indicating the peak location. Constants A, B, C and D govern the bump profile. Values of these parameters are listed in table 1. The bump is designed primarily to envelop the high-sensitivity region and centre around the separation point x_{sep}, featuring a gradual ascent followed by a steep descent. The smooth forward rise prevents additional separation, while the steeper rear section serves to modify the separation bubble. The bump size is relatively small, with a height 15 % of the boundary-layer thickness and a streamwise length 20 % of the separation length. Hereafter, the uncontrolled case is denoted as C_0 and the controlled case as C_{35}, where the subscript denotes the bump height.

The flow response to the introduction of the micro-bump is examined next. Figure 2(*b*) compares the skin-friction coefficient C_f and pressure coefficient C_p. For C_{35}, the bump induces a mild adverse pressure gradient upstream, leading to a minor localised separation ahead of the bump. Near the bump peak, the C_f distribution shows a pronounced increase, while that of C_p exhibits slight fluctuations followed by a recovery. Away from the bump region, both C_f and C_p distributions closely match those of C_0, confirming that the influence of the bump remains highly localised. Over the range $(-10\delta, 8\delta)$, the integrated skin-friction drag of the controlled case C_{35} is reduced by 14 % compared with that of case C_0, while the pressure drag decreases by 0.8 %.

The primary differences emerge in the power spectral density (PSD) spectra near the bump region, as illustrated in figure 2(*c*). Here, we choose the station x_{sep} from case C_0

https://doi.org/10.1017/jfm.2026.11679 Published online by Cambridge University Press

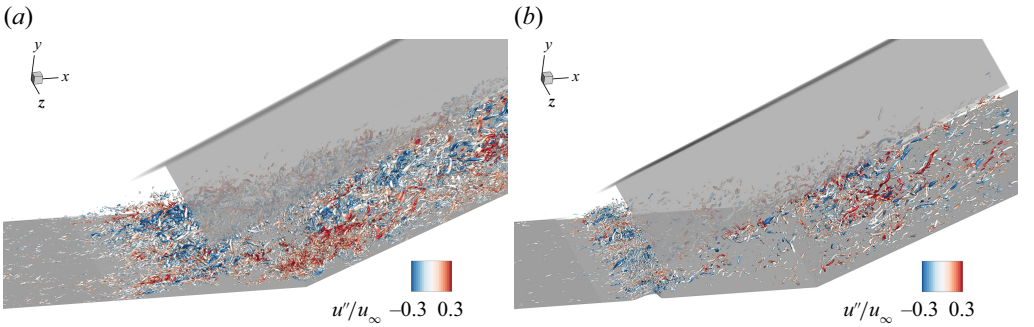


Figure 3. Instantaneous vortices from (*a*) C_0 and (*b*) C_{35}, extracted using the Q-criterion, 5 % of the maximum of C_0, coloured by the Favre-fluctuating velocity u''/u_∞. Transparent iso-surfaces of density-gradient magnitude are used to highlight the shock position.

and x_p from case C_{35} for comparison, where the low-frequency motion is evident. In the low-frequency regime ($St < 0.05$), a predominant peak is observed at $St = 0.031$, which corresponds to the low-frequency breathing motion. However, this peak diminishes in the C_{35} case. With increasing St, high-frequency energy is gradually amplified. A similar trend was also reported by Ceci (2025), where a large shock-control bump was implemented.

A comparison of the instantaneous vortices, coloured by the fluctuating velocity u''/u_∞, is presented in figure 3 for the two cases. Upstream of the separation shock, both cases exhibit negligible vortex activity. In the uncontrolled case C_0, vortices primarily originate near the shock foot and subsequently propagate downstream. While for the controlled C_{35} case, the micro-bump acts as an effective vortex generator, shedding numerous small-scale vortices in its immediate vicinity. Downstream of the bump, the large-scale vortices are significantly reduced compared with case C_0. This distinct alteration in the flow pattern demonstrates that the bump fundamentally modifies the vortex dynamics of the interaction.

The GSA reveals a fundamental change in the 2-D dynamics. As shown in figure 4(*a*), the most unstable 2-D global mode in case C_0 is strongly damped in case C_{35}, transitioning to a stable mode. Its spatial structure also shifts, with high u' amplitudes now concentrated along the shear layer from the bump and the separation shock, rather than at the shock foot, as shown in figure 4(*b*). Although stabilised, this mode is still excited by disturbances through modal resonance. The leading SPOD mode at $St = 0.03$ (figure 4*c*) confirms this, showing strong similarity to the global mode (projection coefficient of 0.89 with the global mode). Crucially, the stable mode is associated with weak breathing motion, as evidenced by the reconstructed unsteady flow fields obtained using the specific SPOD mode (see supplementary movie). Furthermore, the long-time filtered unsteady density gradient magnitude with $St_{cut} = 0.05$ for the two cases is also provided in the supplementary movies, which clearly show weakened shock motion. Convergence of the SPOD modes is verified in Appendix C.

The strength of the low-frequency breathing motion is then quantified and compared for cases C_0 and C_{35}. Here, we compare their wall-normal integrated planar turbulent kinetic energy (TKE) distributions and wall-pressure fluctuations (p'_{rms}). Both quantities are low-pass filtered at $St_{cut} = 0.1$ to focus on the low-frequency dynamics. The planar TKE is defined as follows:

$$\text{Planar TKE} = 0.5 \times \left[\left\langle u''_{span} u''_{span} \right\rangle + \left\langle v''_{span} v''_{span} \right\rangle\right], \tag{3.3}$$

https://doi.org/10.1017/jfm.2026.11679 Published online by Cambridge University Press

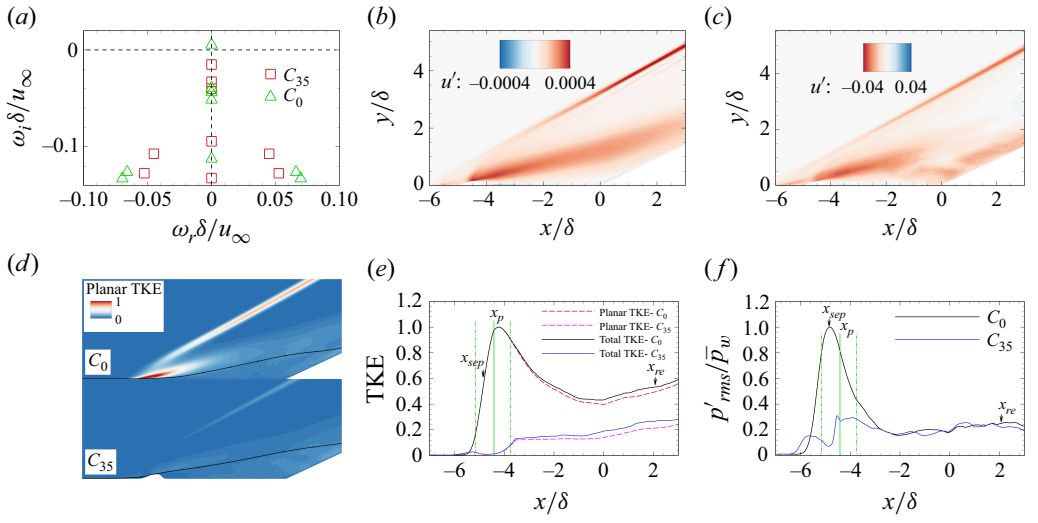


Figure 4. (*a*) Comparison of the eigenvalues for the 2-D modes from cases C_0 and C_{35}. Real parts of (*b*) the 2-D mode and (*c*) the leading SPOD mode at $St = 0.03$ for case C_{35}. (*d*) Low-pass-filtered planar TKE distributions ($St_{cut} = 0.1$), normalised by the square of the friction velocity u_τ^2 at the reference station. Streamwise distributions of (*e*) the wall-normal integrated TKE ($St_{cut} = 0.1$) and (*f*) the normalised wall-pressure root mean square ($St_{cut} = 0.1$) for both cases. Black lines in (*d*) indicate dividing streamlines. Green dash-dot and solid lines in (*c*,*d*) mark the edges and peak positions of the bump, respectively. Both TKE and $p'_{rms}/\bar{p}_w$ in (*e*,*f*) are normalised by the peak values of the C_0 case.

where the spanwise averaging (denoted by the subscript '*span*') and the omission of the small $\langle w''_{span} w''_{span} \rangle$ term are deliberate choices to isolate the dominant 2-D motion from 3-D turbulent fluctuations. This operation is reasonable since the total TKE is mainly contributed by the planar part, as compared in figure 4(*e*). The operator $\langle \cdot \rangle$ signifies the Favre average and the double prime marks the Favre fluctuating variables.

In figure 4(*d*), the filtered TKE distributions of the two cases are presented, normalised by the square of the friction velocity at the reference station and superimposed with the dividing streamlines. In the uncontrolled C_0 case, regions of high TKE are concentrated around the shock foot and along the separation shock, exhibiting a striking resemblance to the structure of the 2-D global mode shown in figure 1(*a*,*b*). This spatial agreement strongly indicates that the low-frequency TKE is governed by this 2-D global mode. In the controlled C_{35} case, the TKE distribution continues to broadly follow the shape of the stabilised global mode from figure 4(*b*,*c*), though with visibly attenuated amplitudes compared to the uncontrolled case.

Figure 4(*e*) compares the streamwise evolutions of the wall-normal integrated TKE for the two cases. For easy comparison, all quantities are normalised by the maximum value obtained in case C_0, and the same normalisation is applied in figure 4(*f*). For case C_0, the TKE begins to rise slightly upstream of x_{sep}, and reaches a peak just downstream of this point, corresponding directly to the high-intensity region observed in the spatial plot. In contrast, the distribution for case C_{35} is fundamentally different. A minor peak with a value of 0.03 occurs upstream of the bump, attributable to the small separation discussed in figure 2(*b*). Within the bump region, the TKE drops to a minimum near the bump peak before increasing again downstream. The peak TKE value in the controlled interaction is approximately 0.15, which is considerably lower than that of the uncontrolled case. Details of this reduction in peak values are presented in table 2. Furthermore, the control effects

https://doi.org/10.1017/jfm.2026.11679 Published online by Cambridge University Press

	St_{cut}	Spatial window	Peak planar TKE	Peak $p'_{rms}/\bar{p}_w$	Averaging interval
C_0	0.1	$(-6\delta, -2\delta)$	1.00 ± 0.0005	1.00 ± 0.001	$553 L_{sep}/u_\infty$
C_{35}	0.1	$(-6\delta, -2\delta)$	0.15 ± 0.0013	0.30 ± 0.0015	$553 L_{sep}/u_\infty$
Reduction	—	—	$85\,\% \pm 0.14\,\%$	$70\,\% \pm 0.18\,\%$	—

Table 2. Performance metrics. For easy comparison, both TKE and $p'_{rms}/\bar{p}_w$ are normalised by the peak values in case C_0.

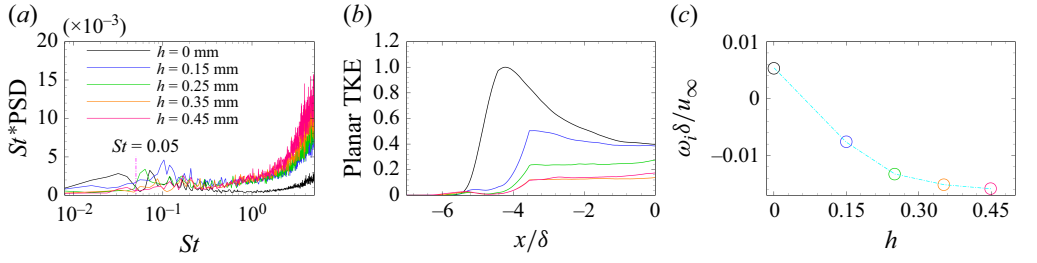


Figure 5. Comparisons of (*a*) pre-multiplied wall-pressure spectra, (*b*) integrated planar TKE ($St_{cut} = 0.1$) and (*c*) the maximum growth rate of the 2-D mode for cases with different bump heights. Streamwise stations in (*a*): x_{sep} for uncontrolled case and x_p for controlled cases.

are independent of the spanwise width, as confirmed by a wider case (8δ) presented in Appendix A.

The control effect is also reflected in the wall-pressure fluctuations $p'_{rms}/\bar{p}_w$ in figure 4(*f*). The C_0 case displays a single, prominent peak near x_{sep}, which decays rapidly downstream and plateaus at around 0.25. The C_{35} case, however, exhibits a bifurcated response with two distinct peaks: one of magnitude 0.15 associated with the upstream separation, and a second peak of 0.3 near the bump peak. Critically, both peaks are substantially weaker than the dominant peak in the uncontrolled flow. Downstream of the bump, the $p'_{rms}/\bar{p}_w$ values stabilise at a level comparable to the uncontrolled case.

Our results confirm that the micro-bump significantly attenuates the low-frequency breathing motion. The control mechanism operates by minimally modifying the base flow, which stabilises the dominant 2-D shock mode and thereby makes it more difficult to be excited by external disturbances. Another plausible explanation is the transformation of the separation mechanism from pressure-induced separation to geometry-induced separation, the latter being associated with comparatively weaker low-frequency dynamics due to the relatively fixed separation point (Eaton & Johnston 1982; Borgmann *et al.* 2024).

Effects of bump height are then investigated. Figure 5(*a*) compares the pre-multiplied wall-pressure spectra for cases with different heights. The low-frequency peak diminishes at $h = 0.15$ mm, indicating that the bump begins to effectively suppress the breathing motion at this height. The low-frequency TKE level drops sharply compared with the uncontrolled case C_0, as seen in figure 5(*b*). Further increasing the bump height has little influence on the spectral shape, but the TKE level continues to decline with height up to $h = 0.35$ mm. At $h = 0.45$ mm, the TKE level is comparable to that at $h = 0.35$ mm, suggesting a local weakening of the suppressive effects. The weakening effects can be explained using the maximum growth rates of the 2-D mode, as illustrated in figure 5(*c*). The growth rate decreases monotonically with bump height, a trend that tends to saturate around $h = 0.45$ mm. In the presence of a bump, the mode shape resembles that shown in

https://doi.org/10.1017/jfm.2026.11679 Published online by Cambridge University Press

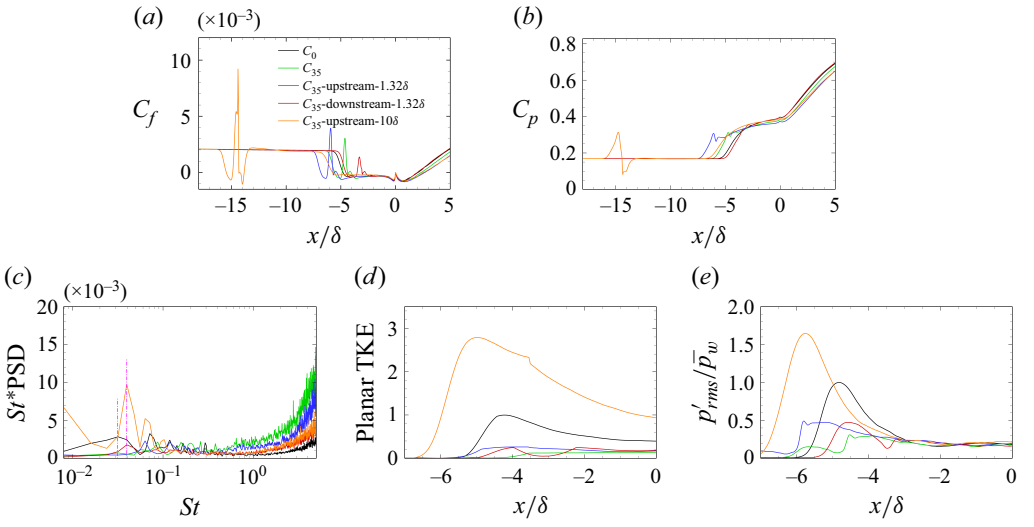


Figure 6. Comparisons of (a,b) C_f and C_p, (c) pre-multiplied wall-pressure spectra, (d) integrated planar TKE ($St_{cut} = 0.1$) and (e) the normalised wall-pressure root mean square ($St_{cut} = 0.1$) of cases at different positions.

figure 4(b). As noted earlier, modal resonance can excite the 2-D mode, which is linked to the weakened breathing motion and can be triggered under modal resonance. Therefore, a sharp reduction in fluctuating energy results from a significantly damped growth rate. If the bump height is increased further, the flow may no longer remain only slightly disturbed and nonlinear effects could emerge, which might in turn reduce the effectiveness of the suppression mechanism.

The effects of bump position are examined by considering three additional cases: case C_{35}–upstream–1.32δ, with the bump shifted 1.32δ upstream; C_{35}–downstream–1.32δ, with the bump shifted 1.32δ downstream; and case C_{35}–upstream–10δ, with the bump shifted 10δ upstream. The first two cases are designed to assess the impact of slight bump shifts, whereas the last case represents a fully off-design condition. Figure 6(a,b) compares the distributions of C_f and C_p for cases at different positions. Large separation bubbles are formed in the two upstream cases, whereas the downstream bump, concealed within the separation bubble, induces only minor changes in the two distributions relative to case C_0. Figure 6(c) shows the pre-multiplied wall-pressure spectra for the original C_0 and C_{35} cases, together with the three repositioned cases. The low-frequency peak is greatly amplified for the fully off-design case (C_{35}–upstream–10δ). For the two slightly shifted cases, the low-frequency components are enhanced compared with the well-controlled C_{35} case, although both remain slightly lower than that in case C_0. The peak TKE and $p'_{rms}/\bar{p}_w$ values increase by 300 % and 150 %, respectively, in the C_{35}–upstream–10δ case. In contrast, the two slightly shifted cases show similar satisfactory reductions in the shock motion strength, with decreases of approximately 75 % in the peak TKE and 50 % in $p'_{rms}/\bar{p}_w$.

The conclusions drawn here regarding positioning the bump far upstream are consistent with Della Posta *et al.* (2024), who reported that an upstream vortex generator amplified the low-frequency magnitude of shock motion. The two partially off-design conditions suggest that slight shifts of the bump can still mitigate the unsteadiness, although the effectiveness varies. Further efforts could employ techniques such as piezoelectrics and

https://doi.org/10.1017/jfm.2026.11679 Published online by Cambridge University Press

shape memory alloys to advance this control strategy towards practical implementation, ensuring the bump remains in the effective region across varying flow conditions.

4. Conclusions

This study employs a micro-bump to suppress the low-frequency unsteadiness in STBLIs through LES and stability analysis. The unsteadiness is shown to be driven by a 2-D global mode, whose instability originates primarily from the shock-foot region. By positioning a micro-bump at this critical region, the 2-D global mode is effectively damped and the local flow dynamics is altered, which substantially weakens the low-frequency motion. The controlled wall-pressure spectrum shows that the energy peak at $St < 0.05$ vanishes, leading to reductions of 85 % in TKE and 70 % in wall-pressure fluctuations associated with $St < 0.1$. These findings highlight the effectiveness of using a micro-bump to mitigate low-frequency unsteadiness, achieving precise suppression with negligible disturbance to the flow and minimal additional drag or other aerodynamic penalties.

The effects of bump height and position are investigated. Effective suppression of breathing motion is achieved once the bump height exceeds $h = 0.15$ mm, and the control effect saturates beyond $h = 0.35$ mm. Furthermore, slightly adjusting the bump position weakens the suppression effects but does not exacerbate the unsteadiness, provided the bump is located near the separation point. These observations may provide useful guidance for practical implementations.

Supplementary movies. Supplementary movies are available at https://doi.org/10.1017/jfm.2026.11679.

Acknowledgements. The authors thank Professor J. Weiss for helpful discussions.

Funding. This work was supported by the National Natural Science Foundation of China under grant 12472239 and the Hong Kong Research Grants Council under grant 15204322.

Declaration of interests. The authors report no conflict of interest.

Appendix A. Effects of the computational width

The effects of computational width are examined in this appendix. For the uncontrolled C_0 case, while the present width cannot resolve large-scale spanwise structures of the order of twice the separation length (Ceci *et al.* 2023; Zhang *et al.* 2025*b*), it is sufficient to capture the dominant 2-D dynamics (Grilli *et al.* 2012; Priebe *et al.* 2016; Pasquariello *et al.* 2017). To verify that the 2-D dynamics is independent of the computational domain width, we compare the original case (spanwise width 4δ) with a wider case (15δ), which includes large-scale 3-D spanwise undulations. As shown in figure 7(*a*), the leading SPOD mode at $St = 0.023$ for the wide case closely resembles the mode in figure 1(*b*). Furthermore, figure 7(*b*) shows that the streamwise distributions of the integrated TKE are nearly identical between the two cases. These comparisons confirm that extending the spanwise width does not alter the fundamental characteristics of the 2-D dynamics.

For the controlled case C_{35}, a wider domain (8δ) is considered. Figures 7(*c*) and 7(*d*) compare the pre-multiplied PSD distributions and the integrated planar TKE profiles between cases with different widths, respectively. The good agreement indicates that the domain width does not influence the control effects. Moreover, the comparison of eigenvalues for cases C_0 and C_{35} with different widths is shown in figure 7(*e*). As expected, variations in width have only a minor influence on the leading few eigenvalues. The impact of the bump on 3-D modes will be addressed in a future study.

https://doi.org/10.1017/jfm.2026.11679 Published online by Cambridge University Press

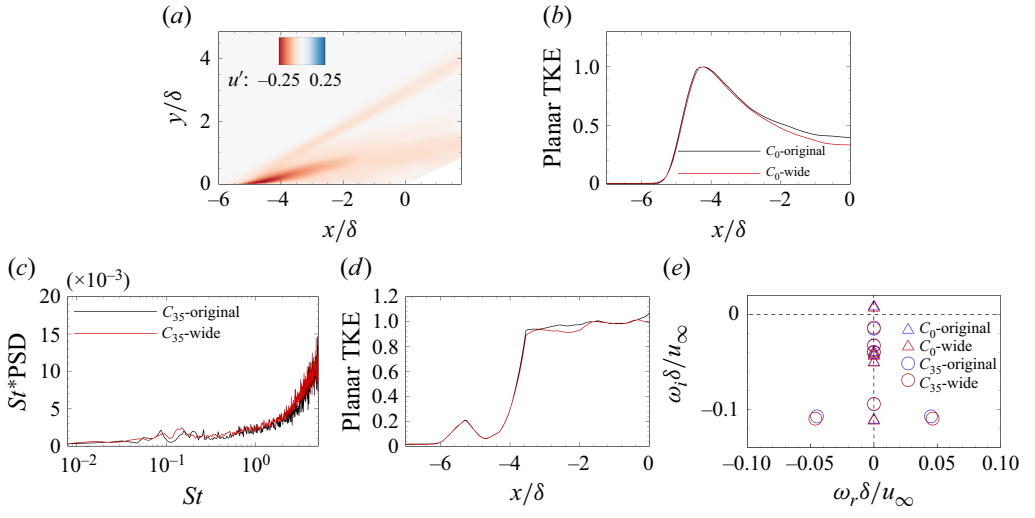


Figure 7. Case C_0: (*a*) real part of the leading 2-D SPOD mode at $St = 0.023$ from the wide case (15δ) and (*b*) wall-normal integrated planar TKE ($St_{cut} = 0.1$) from the original and wide cases, normalised by their respective maxima. Case C_{35}: (*c*) Pre-multiplied wall-pressure spectra and (*d*) planar TKE ($St_{cut} = 0.1$) at different widths (4δ and 8δ), normalised by their respective maxima. (*e*) The comparison of eigenvalues for cases C_0 and C_{35} at different widths.

Appendix B. Eddy viscosity μ_t

The Boussinesq assumption gives

$$-\rho\langle u_i'' u_j''\rangle = -\frac{2}{3}\rho K\delta_{ij} + \left(-\frac{2}{3}\mu_t S_{kk}\delta_{ij} + 2\mu_t S_{ij}\right) \quad (i, j, k \in \{1, 2, 3\}), \tag{B1}$$

where K is the total TKE, S is the Favre-averaged strain-rate tensor and δ_{ij} is the Kronecker delta. Letting $L_{ij} = -\rho\langle u_i'' u_j''\rangle + 2/3\rho K\delta_{ij}$ and $M_{ij} = -1/3 S_{kk}\delta_{ij} + S_{ij}$, the square of the error in (B1) can be defined as (Lilly 1992)

$$Q = \left(L_{ij} - 2\mu_t M_{ij}\right)^2. \tag{B2}$$

Upon setting $\partial Q/\partial\mu_t = 0$, μ_t is evaluated as

$$\mu_t = \frac{1}{2}\left(L_{ij}M_{ij}/M_{ij}^2\right), \tag{B3}$$

which represents the minimum of Q. The least-squares fitting method has been adopted by Abe *et al.* (2012), Coleman, Rumsey & Spalart (2018) and Zhang *et al.* (2025*b*). Regarding the robustness of μ_t in stability analysis, Pickering *et al.* (2021) and Fan *et al.* (2024) systematically discussed different μ_t strategies in resolvent analysis and concluded that the optimal mode is insensitive to the relatively small differences in μ_t when it is represented properly. Hao (2023) demonstrated that although varying RANS models changes the most unstable eigenvalues, the leading modal structures remain consistent. To verify this insensitivity, an alternative μ_t field can be represented using the following formula:

$$\mu_t = C_\mu \rho \frac{K^2}{\epsilon}, \tag{B4}$$

where $C_\mu = 0.09$ and ϵ is the rate of dissipation of TKE (Pope 2001). The corresponding shock mode and sensitivity analysis results are presented in figure 8. The resulting mode

https://doi.org/10.1017/jfm.2026.11679 Published online by Cambridge University Press

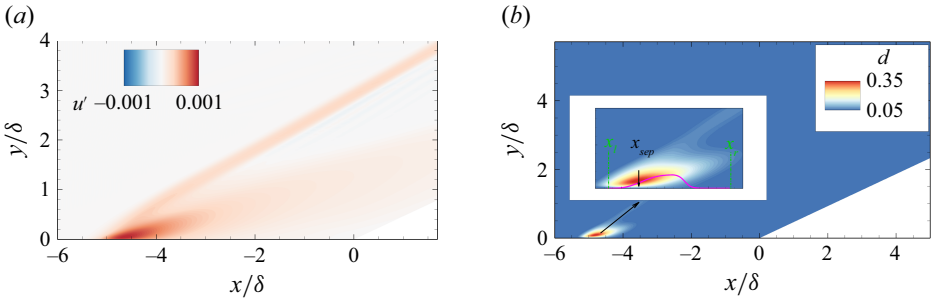


Figure 8. (*a*) Shock mode and (*b*) sensitivity analysis results obtained using the alternative eddy-viscosity model ($\mu_t = C_\mu \rho K^2/\epsilon$).

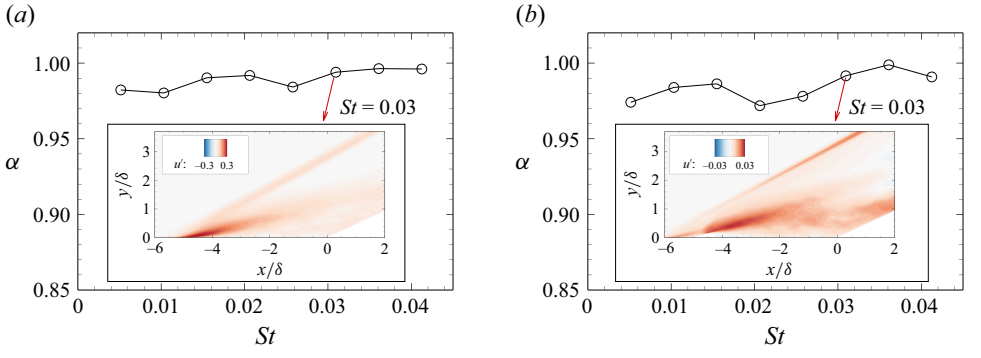


Figure 9. Convergence analysis of (*a*) case C_0 and (*b*) case C_{35}. The insets are from the 75 % dataset.

shape is qualitatively consistent with that shown in figure 1(*a*), and the most sensitive region remains concentrated around the shock foot, aligning with the observations in figure 2(*a*). These comparisons confirm that the linear dynamics is relatively robust with respect to the specific choice of μ_t.

Appendix C. Convergence analysis of SPOD

This appendix aims to verify the convergence of the SPOD modes. Convergence is highly correlated with the number of samples (Lesshafft *et al.* 2019; Schmidt & Colonius 2020). Accordingly, the correlation coefficient α is defined as (Abreu *et al.* 2020; Zhang *et al.* 2025*a*)

$$\alpha = \frac{\left| \| \boldsymbol{\Psi}_{\mathbf{100\,\%}}, \boldsymbol{\Psi}_{\mathbf{75\,\%}} \|_E \right|}{\| \boldsymbol{\Psi}_{\mathbf{100\,\%}} \|_E \times \| \boldsymbol{\Psi}_{\mathbf{75\,\%}} \|_E}, \tag{C1}$$

where $\boldsymbol{\Psi}$ denotes the leading SPOD modes of the first nine frequencies and the subscripts '100 %' and '75 %' indicate the dataset length. A value of 1 indicates a perfect match between the modes from different datasets. Figure 9(*a*,*b*) presents the coefficients from cases C_0 and C_{35}. For all frequencies, values of $\alpha > 0.97$ are obtained. The streamwise velocity perturbations as shown in the insets in figure 9(*a*,*b*) closely resemble those in figures 1(*a*) and 4(*c*). The results based on the 75 % subset show excellent agreement with those from the full 100 % dataset. Hence, the SPOD modes are regarded as converged.

https://doi.org/10.1017/jfm.2026.11679 Published online by Cambridge University Press

References

Abe, H., Mizobuchi, Y., Matsuo, Y. & Spalart, P.R. 2012 DNS and modeling of a turbulent boundary layer with separation and reattachment over a range of Reynolds numbers. *Annu. Res. Briefs* **143**, 311–322.

Abreu, L.I., Cavalieri, A.V.G., Schlatter, P., Vinuesa, R. & Henningson, D.S. 2020 Spectral proper orthogonal decomposition and resolvent analysis of near-wall coherent structures in turbulent pipe flows. *J. Fluid Mech.* **900**, A11.

Anderson, B., Tinapple, J. & Surber, L. 2006 Optimal control of shock wave turbulent boundary layer interactions using micro-array actuation. In *3rd AIAA Flow Control Conference*, p. 3197. American Institute of Aeronautics and Astronautics.

Babinsky, H. & Ogawa, H. 2008 SBLI control for wings and inlets. *Shock Waves* **18** (2), 89–96.

Bernardini, M., Della Posta, G., Salvadore, F. & Martelli, E. 2023 Unsteadiness characterisation of shock wave/turbulent boundary-layer interaction at moderate Reynolds number. *J. Fluid Mech.* **954**, A43.

Borgmann, D., Cura, C., Weiss, J. & Little, J. 2024 Three-dimensional nature of low-frequency unsteadiness in a turbulent separation bubble. *AIAA J.* **62** (11), 4349–4363.

Bruce, P.J.K. & Colliss, S.P. 2015 Review of research into shock control bumps. *Shock Waves* **25** (5), 451–471.

Ceci, A. 2025 Low-frequency unsteadiness mitigation through control bumps in oblique shock wave/boundary-layer interactions. In *AIAA SCITECH 2025 Forum*, p. 2063. American Institute of Aeronautics and Astronautics.

Ceci, A., Palumbo, A., Larsson, J. & Pirozzoli, S. 2023 On low-frequency unsteadiness in swept shock wave–boundary layer interactions. *J. Fluid Mech.* **956**, R1.

Chu, B.-T. 1965 On the energy transfer to small disturbances in fluid flow (Part I). *Acta Mechanica* **1** (3), 215–234.

Clemens, N.T. & Narayanaswamy, V. 2014 Low-frequency unsteadiness of shock wave/turbulent boundary layer interactions. *Annu. Rev. Fluid Mech.* **46** (1), 469–492.

Coleman, G.N., Rumsey, C.L. & Spalart, P.R. 2018 Numerical study of turbulent separation bubbles with varying pressure gradient and Reynolds number. *J. Fluid Mech.* **847**, 28–70.

Della Posta, G., Martelli, E., Salvadore, F. & Bernardini, M. 2024 High-fidelity simulations of microramp-controlled shock wave/boundary layer interaction. *J. Fluid Mech.* **998**, A12.

Dolling, D.S. 2001 Fifty years of shock-wave/boundary-layer interaction research: what next? *AIAA J.* **39** (8), 1517–1531.

Eaton, J.K. & Johnston, J.P. 1982 Low frequency unsteadyness of a reattaching turbulent shear layer. In *Turbulent Shear Flows 3: Selected Papers from the Third International Symposium on Turbulent Shear Flows*, pp. 162–170. Springer.

Fan, Y., Kozul, M., Li, W. & Sandberg, R.D. 2024 Eddy-viscosity-improved resolvent analysis of compressible turbulent boundary layers. *J. Fluid Mech.* **983**, A46.

Fang, J., Zheltovodov, A.A., Yao, Y., Moulinec, C. & Emerson, D.R. 2020 On the turbulence amplification in shock-wave/turbulent boundary layer interaction. *J. Fluid Mech.* **897**, A32.

Ghosh, S., Choi, J.-I. & Edwards, J. 2008 RANS and hybrid LES/RANS simulation of the effects of micro vortex generators using immersed boundary methods. In *38th Fluid Dynamics Conference and Exhibit*, p. 3728. American Institute of Aeronautics and Astronautics.

Grilli, M., Schmid, P.J., Hickel, S. & Adams, N.A. 2012 Analysis of unsteady behaviour in shockwave turbulent boundary layer interaction. *J. Fluid Mech.* **700**, 16–28.

Hao, J. 2023 On the low-frequency unsteadiness in shock wave–turbulent boundary layer interactions. *J. Fluid Mech.* **971**, A28.

Hao, J. & Wen, C.-Y. 2020 Hypersonic flow over spherically blunted double cones. *J. Fluid Mech.* **896**, A26.

Jameson, A., Schmidt, W. & Turkel, E. 1981 Numerical solution of the Euler equations by finite volume methods using runge kutta time stepping schemes. In *14th Fluid and Plasma Dynamics Conference*, p. 1259. American Institute of Aeronautics and Astronautics.

Jiang, G.-S. & Shu, C.-W. 1996 Efficient implementation of weighted ENO schemes. *J. Comput. Phys.* **126** (1), 202–228.

Jung, J., Bhagwat, R. & Towne, A. 2025 Resolvent-based estimation and control of a laminar airfoil wake. *J. Fluid Mech.* **1016**, A41.

Lesshafft, L., Semeraro, O., Jaunet, V., Cavalieri, A.V.G. & Jordan, P. 2019 Resolvent-based modeling of coherent wave packets in a turbulent jet. *Phys. Rev. Fluids* **4** (6), 063901.

Lilly, D.K. 1992 A proposed modification of the Germano subgrid-scale closure method. *Phys. Fluids A: Fluid Dyn.* **4** (3), 633–635.

Liou, M.-S. 2006 A sequel to AUSM, part II: AUSM+-up for all speeds. *J. Comput. Phys.* **214** (1), 137–170.

https://doi.org/10.1017/jfm.2026.11679 Published online by Cambridge University Press

LIU, X., CHEN, L., ZHANG, Y., TAN, H., LIU, Y. & PENG, D. 2024 Spanwise unsteadiness in the sidewall-confined shock-wave/boundary-layer interaction. *J. Fluid Mech.* **987**, R6.

MANI, A. 2012 Analysis and optimization of numerical sponge layers as a nonreflective boundary treatment. *J. Comput. Phys.* **231** (2), 704–716.

MARQUET, O., SIPP, D. & JACQUIN, L. 2008 Sensitivity analysis and passive control of cylinder flow. *J. Fluid Mech.* **615**, 221–252.

MARTINEZ-CAVA, A., CHÁVEZ-MODENA, M., VALERO, E., DE VICENTE, J. & FERRER, E. 2020 Sensitivity gradients of surface geometry modifications based on stability analysis of compressible flows. *Phys. Rev. Fluids* **5** (6), 063902.

NASTRO, G., ROBINET, J.-C., LOISEAU, J.-C., PASSAGGIA, P.-Y. & MAZELLIER, N. 2023 Global stability, sensitivity and passive control of low-Reynolds-number flows around NACA 4412 swept wings. *J. Fluid Mech.* **957**, A5.

NICHOLS, J.W., LARSSON, J., BERNARDINI, M. & PIROZZOLI, S. 2017 Stability and modal analysis of shock/boundary layer interactions. *Theor. Comput. Fluid Dyn.* **31** (1), 33–50.

PALADINI, E., MARQUET, O., SIPP, D., ROBINET, J.-C. & DANDOIS, J. 2019 Various approaches to determine active regions in an unstable global mode: application to transonic buffet. *J. Fluid Mech.* **881**, 617–647.

PASQUARIELLO, V., HICKEL, S. & ADAMS, N.A. 2017 Unsteady effects of strong shock-wave/boundary-layer interaction at high Reynolds number. *J. Fluid Mech.* **823**, 617–657.

PICKERING, E., RIGAS, G., SCHMIDT, O.T., SIPP, D. & COLONIUS, T. 2021 Optimal eddy viscosity for resolvent-based models of coherent structures in turbulent jets. *J. Fluid Mech.* **917**, A29.

PIROZZOLI, S. 2010 Generalized conservative approximations of split convective derivative operators. *J. Comput. Phys.* **229** (19), 7180–7190.

POPE, S.B. 2001 Turbulent flows. *Meas. Sci. Technol.* **12** (11), 2020–2021.

PRIEBE, S., TU, J.H., ROWLEY, C.W. & MARTÍN, M.P. 2016 Low-frequency dynamics in a shock-induced separated flow. *J. Fluid Mech.* **807**, 441–477.

RIBEIRO, J.H.M. & TAIRA, K. 2024 Triglobal resolvent-analysis-based control of separated flows around low-aspect-ratio wings. *J. Fluid Mech.* **995**, A13.

SCHMIDT, O.T. & COLONIUS, T. 2020 Guide to spectral proper orthogonal decomposition. *AIAA J.* **58** (3), 1023–1033.

SOUVEREIN, L.J., DUPONT, P., DEBIEVE, J.-F., DUSSAUGE, J.-P., VAN, O., BAS, W. & SCARANO, F. 2010 Effect of interaction strength on unsteadiness in shock-wave-induced separations. *AIAA J.* **48** (7), 1480–1493.

SUN, D., GUO, Q., LI, C. & LIU, P. 2019 Direct numerical simulation of effects of a micro-ramp on a hypersonic shock wave/boundary layer interaction. *Phys. Fluids* **31** (12), 126101.

TOUBER, E. & SANDHAM, N.D. 2009 Large-eddy simulation of low-frequency unsteadiness in a turbulent shock-induced separation bubble. *Theor. Comput. Fluid Dyn.* **23**, 79–107.

ZHANG, Z., HAO, J. & UY, K.C.K. 2025*a* Characterising görtler vortices in supersonic turbulent flows over concave surfaces. *J. Fluid Mech.* **1012**, A29.

ZHANG, Z., LI, X. & HAO, J. 2025*b* Analysis of large-scale spanwise motions in shock wave–turbulent boundary-layer interactions. *J. Fluid Mech.* **1018**, A2.

https://doi.org/10.1017/jfm.2026.11679 Published online by Cambridge University Press